



# Possible Habitats for NH<sub>3</sub>, NH<sub>2</sub>D, H<sup>13</sup>CN, HC<sup>15</sup>N, SO, and C<sup>18</sup>O in the Initial Conditions of High-mass Star Formation

Quan-Ling Cui<sup>1,2,3</sup>, Chuan-Peng Zhang<sup>1,4</sup>, and Jun-Jie Wang<sup>1</sup>

<sup>1</sup> National Astronomical Observatories, Chinese Academy of Sciences, Beijing 100101, China; [cpzhang@nao.cas.cn](mailto:cpzhang@nao.cas.cn)

<sup>2</sup> University of Chinese Academy of Sciences, Beijing 100049, China

<sup>3</sup> College of Science, Qiqihar University, Qiqihar 161006, China

<sup>4</sup> Guizhou Radio Astronomical Observatory, Guizhou University, Guiyang 550000, China

Received 2024 January 15; revised 2024 March 13; accepted 2024 March 26; published 2024 April 24

## Abstract

The initial condition of high-mass star formation is a complex area of study because of the high densities ( $n_{\text{H}_2} > 10^6 \text{ cm}^{-3}$ ) and low temperatures ( $T_{\text{dust}} < 18 \text{ K}$ ) involved. Under such conditions, many molecules become depleted from the gas phase by freezing out onto dust grains. However, the N-bearing and deuterated species could remain gaseous under these extreme conditions, suggesting that they may serve as ideal tracers. In this paper, using the Plateau de Bure Interferometer and Very Large Array observations at 1.3 mm, 3.5 mm, and 1.3 cm, we investigate the possible habitats for NH<sub>3</sub>, NH<sub>2</sub>D, H<sup>13</sup>CN, HC<sup>15</sup>N, SO, and C<sup>18</sup>O in eight massive precluster and protocluster clumps G18.17, G18.21, G23.97N, G23.98, G23.44, G23.97S, G25.38, and G25.71. We found that the NH<sub>3</sub> cores are in good agreement with the 3.5 mm peak emission, but the NH<sub>3</sub> is much more extended than the 3.5 mm emission structure. The SO distributions agree well with the 3.5 mm peaks for the evolved star formation stage, but we did not detect any SO emission in the four earliest star formation sources. C<sup>18</sup>O is a poor tracer in conditions of the cold ( $\lesssim 18 \text{ K}$ ) and dense ( $\gtrsim 10^4 \text{ cm}^{-3}$ ) cores, e.g., the prestellar cores. We also found that the NH<sub>2</sub>D cores are mainly located in the temperature range of 13.0–20.0 K, and the NH<sub>2</sub>D lines may be strongly depleted above 20 K.

**Key words:** galaxies: star formation – techniques: interferometric – methods: observational

## 1. Introduction

High-mass star formation with larger than  $8 M_{\odot}$  dominates the environment and evolution of the Galaxy. However, there is still a lack of knowledge about how high-mass stars form in their early stages (e.g., Pillai et al. 2007, 2011, 2012; Motte et al. 2018; Zhang et al. 2019, 2020). Particularly, the transition from a prestellar core to a protostar has not been well studied observationally due to the short lifetime of the prestellar stage, the difficulty in determining the relative evolutionary stage of the objects, the small spatial scales involved, and the lack of strong molecular tracers of cores at high densities (Friesen et al. 2014). At the high densities ( $n_{\text{H}_2} > 10^6 \text{ cm}^{-3}$ ) and low temperatures ( $T_{\text{dust}} < 18 \text{ K}$ ) characteristic of the interiors of highly evolved star-forming cores, many molecules deplete from the gas phase by freezing onto dust grains (Walmsley et al. 2004; Bergin & Tafalla 2007), even the dense tracer C<sup>18</sup>O (Zhang et al. 2017). However, some N-bearing species are good tracers of dense gas and cold conditions toward initial star formation. In addition, the deuterium fraction of the remaining gas phase species increases dramatically above the cosmic abundance ratio ( $[\text{D}/\text{H}] \sim 1.5 \times 10^{-5}$ ; Oliveira et al. 2003) due to the increased production of H<sub>2</sub>D<sup>+</sup> by the reaction of H<sub>3</sub><sup>+</sup> with HD in places where CO is depleted (Roberts & Millar 2000).

The elements C, N, O, and S, produced by nucleosynthesis in stars, are the important components in the early star formation of the Galaxy (e.g., Wilson & Rood 1994; Wielen & Wilson 1997; Ikeda et al. 2002). The abundances of C, N, and O may contain important information not only about the history of nucleosynthesis, but also about the earliest stages of star formation. Understanding their precise content in local interstellar clouds is of fundamental importance in astrophysics and astrochemistry (e.g., Gerner 2014; Gerner et al. 2015). The elements have been widely observed in many different observations, such as in the form of CO, SO, HCN, and NH<sub>3</sub> (e.g., Zhang et al. 2014, 2017). However, their isotopic species, such as SO, H<sup>13</sup>CN, HC<sup>15</sup>N, and NH<sub>2</sub>D (e.g., Daniel et al. 2016; Booth et al. 2019; Li et al. 2024) in the early stage of massive star formation, are rarely studied in detail.

Investigating different molecular tracers in different star formation environments is helpful to tell us how to select and use an appropriate tracer to study a particular star formation condition. Thus, in this paper we mainly investigate the possible habitats for NH<sub>3</sub>, NH<sub>2</sub>D, H<sup>13</sup>CN, HC<sup>15</sup>N, SO, and C<sup>18</sup>O associated with the early stage of high-mass star formation. In addition, in Section 2 we present the associated observations and data reduction. In Section 3 we present the

observational results and analysis for the 3.5 mm continuum emission, NH<sub>3</sub>, NH<sub>2</sub>D, H<sup>13</sup>CN, HC<sup>15</sup>N, SO, and C<sup>18</sup>O spectra. In Section 4 we discuss possible habitats for NH<sub>2</sub>D and the other N-bearing species. A summary is given in Section 5.

## 2. Observations and Data Reduction

### 2.1. General Observational Information

The IRAM<sup>5</sup> Plateau de Bure Interferometer (PdBI) and National Radio Astronomy Observatory (NRAO)<sup>6</sup> Very Large Array (VLA) observations in the 1.3 mm, 3.5 mm, and 1.3 cm continuum toward the clumps G18.17, G18.21, G23.97N, G23.98, G23.44, G23.97S, G25.38, and G25.71 have been described and presented in Zhang et al. (2019). The NH<sub>2</sub>D 1<sub>11</sub>–1<sub>01</sub> (at 85.926 GHz), NH<sub>3</sub> (1, 1), and (2, 2) observations have been presented in Zhang et al. (2020). Here the spectral observations and data, including H<sup>13</sup>CN, HC<sup>15</sup>N, SO, and C<sup>18</sup>O, combined with the above data, are further described and exhibited. Additionally, in this paper, only the 3.5 mm continuum data are used to trace the dense cores in the clumps. The 1.3 cm continuum data, which mainly trace the free–free emission, are not used in this paper; 1.3 mm continuum data, which have relatively much smaller effective regions and lower sensitivity than 3.5 mm continuum data, are also not used in this work.

### 2.2. PdBI Observations

The spectra in the PdBI observations were observed simultaneously with the continuum, but with separate correlator windows. In receiver 1, NH<sub>2</sub>D (85.926 GHz) and H<sup>13</sup>CN (86.340 GHz) were each tuned to a 40 MHz bandwidth with 460 channels having a velocity resolution of 0.27 km s<sup>-1</sup> per channel; HC<sup>15</sup>N (86.055 GHz) and SO (86.094 GHz) were tuned to the same 80 MHz bandwidth with 230 channels having a velocity resolution of 1.09 km s<sup>-1</sup> per channel. In receiver 2, C<sup>18</sup>O (219.560 GHz) was tuned to an 80 MHz bandwidth with 230 channels, which has a velocity resolution of 0.43 km s<sup>-1</sup> per channel. The rms noise of the spectra was about 23 mJy beam<sup>-1</sup> for NH<sub>2</sub>D on the CD track and about 12 mJy beam<sup>-1</sup> for NH<sub>2</sub>D on the BCD track. In this work, we only used the observational data on the CD track.

The IRAM software package GILDAS<sup>7</sup> was utilized for spectral reduction. The region of a double primary beam was searched for cleaning components. No polygon was introduced to avoid any biased cleaning. The primary beam is 58''.5 and 23''.0 at 86.086 and 219.560 GHz, respectively. The data have

<sup>5</sup> IRAM is supported by INSU/CNRS (France), MPG (Germany) and IGN (Spain).

<sup>6</sup> The National Radio Astronomy Observatory is a facility of the National Science Foundation operated under cooperative agreement by Associated Universities, Inc.

<sup>7</sup> <http://www.iram.fr/IRAMFR/GILDAS/>

been corrected for primary beam attenuation. More details are presented in Zhang et al. (2019, 2020).

## 3. Observational Results and Analysis

For eight clumps G18.17, G18.21, G23.97N, G23.98, G23.44, G23.97S, G25.38, and G25.71, the maps for NH<sub>3</sub>, NH<sub>2</sub>D, H<sup>13</sup>CN, HC<sup>15</sup>N, SO, C<sup>18</sup>O, and the 3.5 mm continuum emission are shown in Appendix, while the maps for the kinetic temperature and column density can be found in Zhang et al. (2019, 2020). The clumps G18.17, G18.21, G23.97N, and G23.98 are in an early star formation stage or prestellar stage, while the clumps G23.44, G23.97S, G25.38, and G25.71 are in an evolved star formation stage or protostar stage (Zhang et al. 2019). We use the function `scipy.stats.binned_statistic()` in Python to count the pixel-by-pixel relationships between the tracers NH<sub>3</sub>, NH<sub>2</sub>D, H<sup>13</sup>CN, HC<sup>15</sup>N, SO, and C<sup>18</sup>O and the 3.5 mm continuum emission, kinetic temperature, and column density. Each parameter space (from minimum to maximum) is divided into 20 bins. The minimum and the maximum of each parameter space can be seen in Figures 2–8, where we plotted some relationships of the tracers. In these figures above, the integrated intensities for the NH<sub>3</sub>, NH<sub>2</sub>D, H<sup>13</sup>CN, HC<sup>15</sup>N, SO, and C<sup>18</sup>O data are the averaged value in the given bin. Moreover, the 3.5 mm continuum emission, kinetic temperature, and column density are relative values that have been normalized. The correlation for each tracer is shown below.

### 3.1. NH<sub>3</sub> (1, 1) and (2, 2)

We further present the NH<sub>3</sub> (1, 1) and (2, 2) spectral example shown in Figure 1 and integrated intensity maps displayed in Appendix. We mainly use the NH<sub>3</sub> data to show the distributions of the column density and kinetic temperature of dense cores. The calculations have been introduced in detail in Zhang et al. (2019, 2020). Furthermore, Zhang et al. (2020) presented the optical depth relations between NH<sub>2</sub>D and NH<sub>3</sub> (1, 1). We can see that most of the NH<sub>3</sub> (1, 1) cores have optical depth ranging from 1.5 to 9, indicating that these molecular clouds are often optically thick for NH<sub>3</sub> (1, 1). The optical depth of NH<sub>2</sub>D ranges from 0.1 to 9.7, most of which are more than 1, thus NH<sub>2</sub>D is usually optically thick in dense and cold cores. In Figures 2 and 3 we can see that the relationships between the NH<sub>3</sub>(1, 1), (2, 2) and the 3.5 mm continuum emission and column density are positively correlated for most of the sources. However, there is no obvious relationship between NH<sub>3</sub>(1, 1), (2, 2) and the kinetic temperature. In Figures A1 and A2, we can see also that the NH<sub>3</sub> peak position is well consistent with that of the 3.5 mm emission, but the NH<sub>3</sub> is much more extended than the 3.5 mm emission structure. However, the NH<sub>3</sub>(1, 1), (2, 2) distributions are more extended than the 3.5 mm emission distributions.

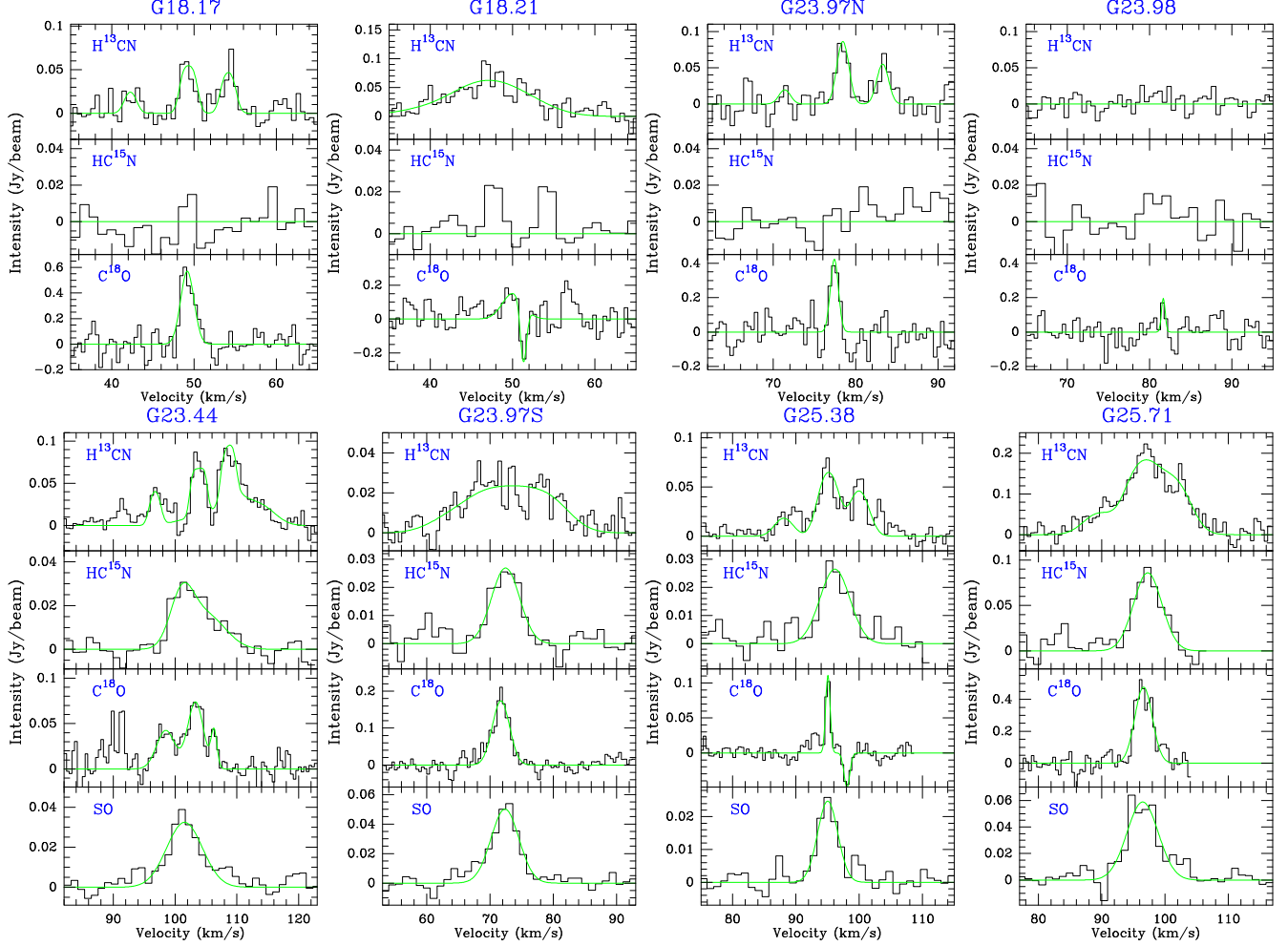


**Figure 1.** Example for spectra of  $\text{H}^{13}\text{CN}$ ,  $\text{HC}^{15}\text{N}$ ,  $\text{C}^{18}\text{O}$ , and  $\text{SO}$  extracted from the most massive 3.5 mm continuum cores (see the 3.5 mm continuum cores in Zhang et al. 2019). The green curves simply represent the line emission fit for each spectrum.

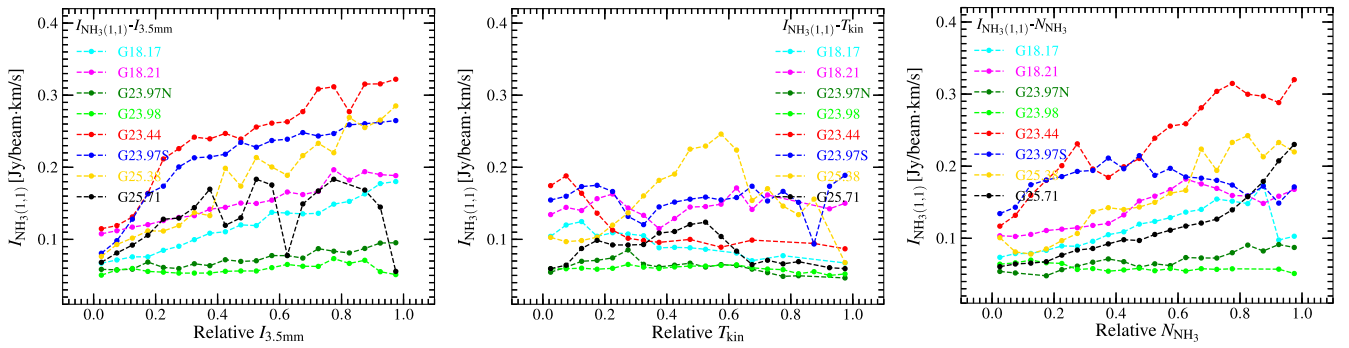


**Figure 2.** Binned  $\text{NH}_3(1,1)$  integrated intensity distributions vs. related 3.5 mm continuum emission, kinetic temperature, and  $\text{NH}_3$  column density distributions.

### 3.2. $\text{NH}_2\text{D}$ at 85.926 GHz

We further present the  $\text{NH}_2\text{D}$  integrated intensity maps in Appendix. Zhang et al. (2020) found that the  $\text{NH}_2\text{D}$  cores have a colder state than these continuum cores, and most of the  $\text{NH}_2\text{D}$  cores have a temperature between 13 and 17 K with only

a few of the  $\text{NH}_2\text{D}$  cores having kinetic temperatures above 20 K. It is likely that these cores with  $\gtrsim 20$  K are just ahead of the deeply embedded cores with  $\gtrsim 20$  K in line of sight. The derived kinetic temperatures may be contaminated by background emission, and the  $\text{NH}_2\text{D}$  is just tracing the envelope of

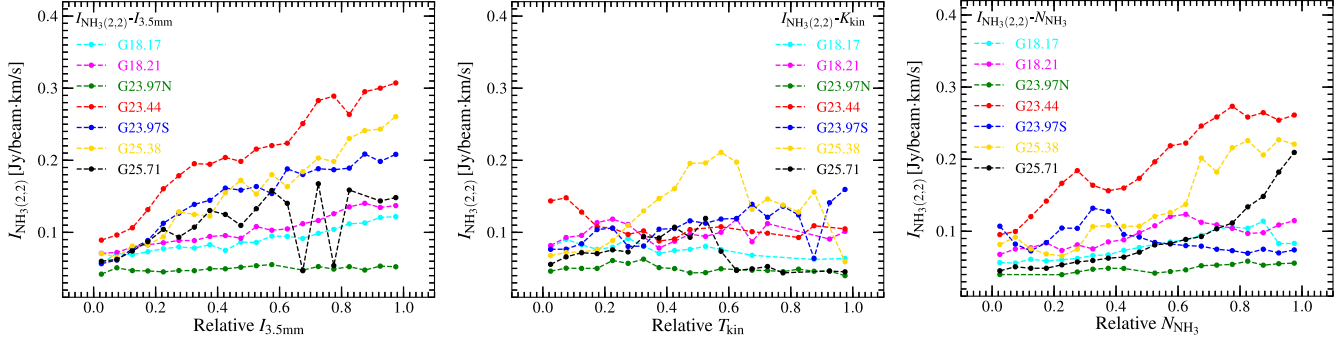


**Figure 3.** Binned  $\text{NH}_3(2,2)$  integrated intensity distributions vs. related 3.5 mm continuum emission, kinetic temperature, and  $\text{NH}_3$  column density distributions.

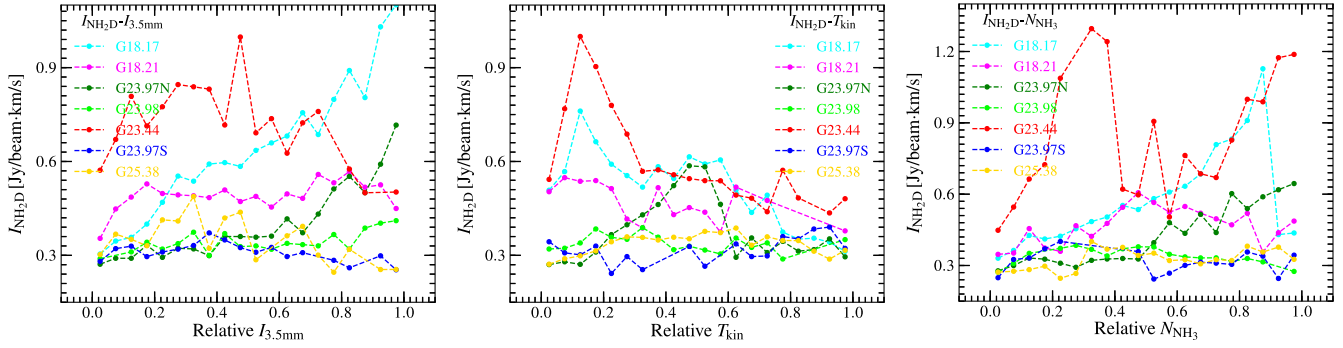


**Figure 4.** Binned  $\text{NH}_2\text{D}$  integrated intensity distributions vs. related 3.5 mm continuum emission, kinetic temperature, and  $\text{NH}_3$  column density distributions.

the cores with  $\gtrsim 20$  K. Therefore, the  $\text{NH}_2\text{D}$  lines may be depleted above 20 K. Comparing the column densities between  $\text{NH}_2\text{D}$  and continuum cores, we found that the  $\text{NH}_2\text{D}$  distributions are in a relatively diffuse condition compared to the continuum cores. Therefore, the  $\text{NH}_2\text{D}$  line may be a good tracer of prestellar cores. In Figure 4 we can see that there is an anti-correlation between the  $\text{NH}_2\text{D}$  and the kinetic temperature, but these are positively correlated for the sources G18.17, G23.44, and G18.21, while the relationship is not obvious for the other sources. In addition, the relationship between the  $\text{NH}_2\text{D}$  and the 3.5 mm continuum is also not obvious, but there is a weak positive correlation between the  $\text{NH}_2\text{D}$  and the column density. The possible reasons for this are discussed in detail in Section 4.1.

### 3.3. $\text{H}^{13}\text{CN}$ at 86.340 GHz

$\text{H}^{13}\text{CN}$  often traces dense and cold cores. Spectra of  $\text{H}^{13}\text{CN}$  have three hyperfine structure (HFS) lines (see Figure 1) (Csengeri et al. 2011; Padovani et al. 2011). The  $\text{H}^{13}\text{CN}$  spectra of the most massive core among 3.5 mm continuum cores are shown in Figure 1. In Figure 5 we find that the relationships between the  $\text{H}^{13}\text{CN}$  integrated intensity and the related 3.5 mm continuum emission, kinetic temperature, and  $\text{NH}_3$  column density distributions are positively correlated for

most sources. The integrated-intensity contours are superimposed on the 3.5 mm emission image in Figure A5. We can see that the  $\text{H}^{13}\text{CN}$  emission is compact and surrounds the 3.5 mm emission. It is likely that  $\text{H}^{13}\text{CN}$  often traces dense and cold cores for the 3.5 mm emission.

### 3.4. $\text{HC}^{15}\text{N}$ at 86.055 GHz

The  $\text{HC}^{15}\text{N}$  spectra of the most massive core among 3.5 mm continuum cores are shown in Figure 1. The integrated-intensity contours are superimposed on the 3.5 mm emission image in Figure A6. The  $\text{HC}^{15}\text{N}$  distributions are well consistent with the 3.5 mm peaks. The cores within clumps G23.44, G23.97S, G25.38, and G25.71 are more evolved than those in clumps G18.17, G18.21, G23.97N, and G23.98, and the most massive cores have a relatively higher temperature condition than the surrounding cores (Zhang et al. 2019). Therefore, it is likely that the  $\text{HC}^{15}\text{N}$  traces the evolved conditions, and the distributions of  $\text{HC}^{15}\text{N}$  emissions are only concentrated close to warmer condition within each source. In Figure 6 we find that the relationships between the related 3.5 mm continuum,  $\text{NH}_3$  column density distributions, and the  $\text{HC}^{15}\text{N}$  integrated intensity are positively correlated for most sources, but we cannot see a correlation between the kinetic

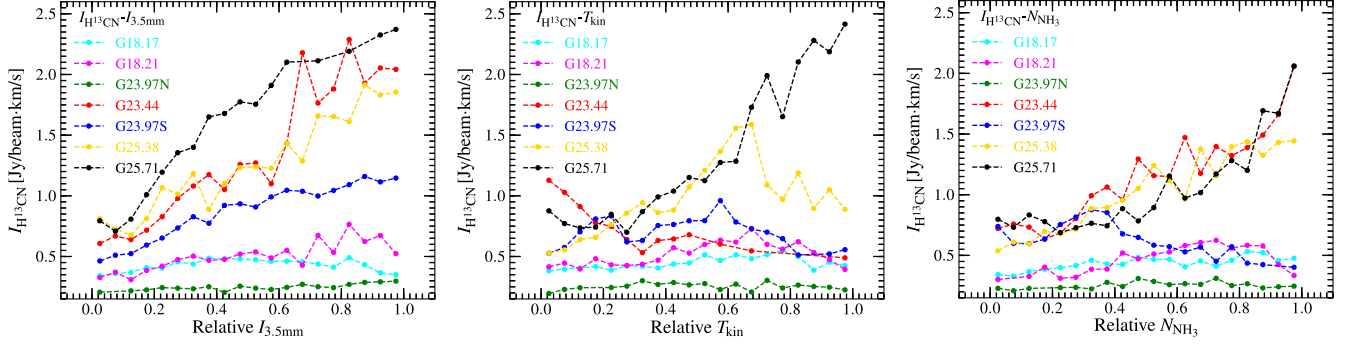


**Figure 5.** Binned  $\text{H}^{13}\text{CN}$  integrated intensity distributions vs. related 3.5 mm continuum emission, kinetic temperature, and  $\text{NH}_3$  column density distributions.

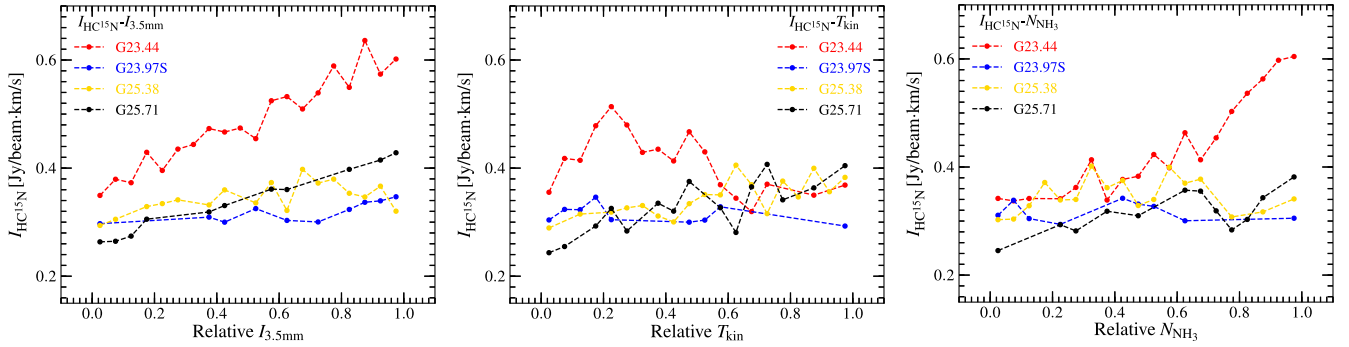


**Figure 6.** Binned  $\text{HC}^{15}\text{N}$  integrated intensity distributions vs. related 3.5 mm continuum emission, kinetic temperature, and  $\text{NH}_3$  column density distributions.

temperature and the  $\text{HC}^{15}\text{N}$  integrated intensity. This indicates that the  $\text{HC}^{15}\text{N}$  is not a good temperature tracer.

### 3.5. SO at 86.094 GHz

The SO spectra of the most massive core among 3.5 mm continuum cores are shown only for sources G23.44, G23.97S, G25.38, and G25.71 in Figure 1, because we did not detect any SO emission at the other four sources. The integrated-intensity contours are superimposed on a 3.5 mm emission image in Figure A7. The SO distributions are well consistent with the 3.5 mm peaks, except that the peak for G25.38 is offset from 3.5 mm emission. This molecule, SO, appears to be less confined to a small region than others. In Figure 7 we can see that there is an obvious positive correlation between the SO integrated intensity and the 3.5 mm continuum distributions. For the kinetic temperature and column density we do not see any obvious relationships.

### 3.6. $\text{C}^{18}\text{O}$ at 219.560 GHz

The  $\text{C}^{18}\text{O}$  spectra of the most massive core among 3.5 mm continuum cores are shown in Figure 1.  $\text{C}^{18}\text{O}$  emissions have been superimposed on the 3.5 mm continuum in Figure A8, where the primary beam of  $\text{C}^{18}\text{O}$  is the dotted circle. Most of

the  $\text{C}^{18}\text{O}$  emission is available at or near the 3.5 mm peaks because of the warmer conditions or more evolved condition there. It is quite rare that the  $\text{NH}_2\text{D}$  cores are located at the positions of the  $\text{C}^{18}\text{O}$  emissions. Therefore,  $\text{C}^{18}\text{O}$  is susceptible to be severely depleted at low temperatures ( $\leq 20$  K) and high densities. In Figure 8 we can see a positive correlation between the  $\text{C}^{18}\text{O}$  integrated intensity and column density distributions only for source G23.44, while for other sources the relationships are not obvious. The main reason for this may be that the  $\text{C}^{18}\text{O}$  is optically thick and has been frozen to the dust grain surface in the dense and cold condition (e.g., Zhang et al. 2017). Generally, we suggest that the  $\text{C}^{18}\text{O}$  could be used to study the diffuse ( $\lesssim 10^4 \text{ cm}^{-3}$ ) and warm ( $\gtrsim 20$  K) star formation regions.

## 4. Discussion

### 4.1. $\text{NH}_2\text{D}$ Distribution

$\text{NH}_2\text{D}$  may form in different ways, for example, the deuterated ions trace the place of hydrogen in the ammonia in the gas phase, and in cold areas ( $\lesssim 20$  K),  $\text{H}_2\text{D}^+$  reacts with  $\text{NH}_3$  to generate  $\text{NH}_2\text{D}$  (e.g., Rodgers & Charnley 2001; Caselli et al. 2008; Caselli & Ceccarelli 2012; Ceccarelli et al. 2014). Li et al. (2024) presented  $\text{NH}_2\text{D}$  mapping in a

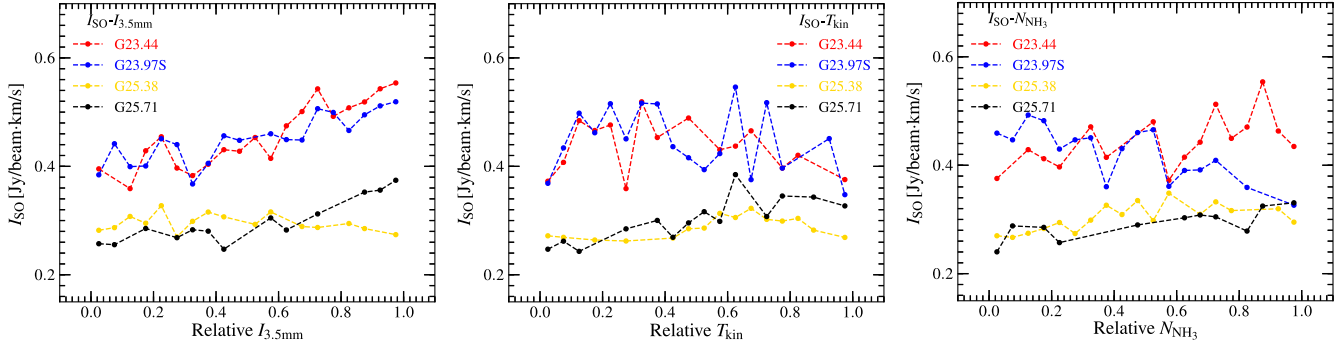


**Figure 7.** Binned SO integrated intensity distributions vs. related 3.5 mm continuum emission, kinetic temperature, and  $\text{NH}_3$  column density distributions.

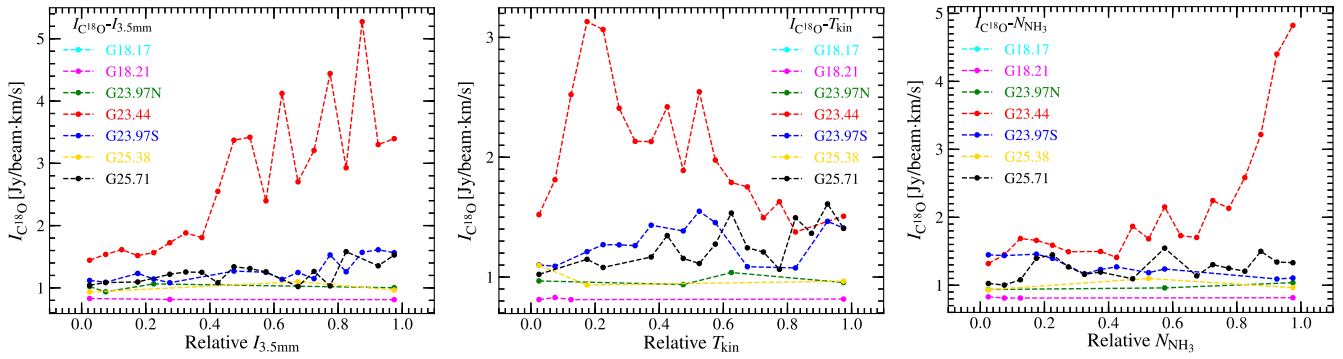


**Figure 8.** Binned  $\text{C}^{18}\text{O}$  integrated intensity distributions vs. related 3.5 mm continuum emission, kinetic temperature, and  $\text{NH}_3$  column density distributions.

sample of 24 late-stage massive star-forming regions using the IRAM 30 m, and found that  $\text{NH}_2\text{D}$  emissions have a complex distribution. They suggest that the dense gas (or gas density) may not be an important physical parameter to affect the  $\text{NH}_2\text{D}$  enhancement in these targets, compared with other physical parameters (such as temperature). However, this may be biased due to their limited spatial resolution and sensitivity.

In this work, we found that  $\text{NH}_2\text{D}$  cores have quite narrow line widths, half of which are below  $1.0 \text{ km s}^{-1}$  (see Zhang et al. 2020), indicating a very small velocity dispersion for  $\text{NH}_2\text{D}$  cores. Little  $\text{NH}_2\text{D}$  emission is detected toward the continuum cores, but we detected  $\text{NH}_3$  lines for most of the cores (see Figure A4). Based on this, we can compare the velocity dispersion between  $\text{NH}_2\text{D}$  and continuum cores (see Zhang et al. 2019, 2020). We found that the continuum cores have a larger velocity dispersion than the  $\text{NH}_2\text{D}$  cores. The thermal broadening of the spectra is very small at the rotational temperature below 20 K, so the turbulent conditions of the  $\text{NH}_2\text{D}$  cores are relatively quiescent.

For the eight samples in Figures A1 and A3, we superimposed  $\text{NH}_2\text{D}$  and  $\text{NH}_3$  contours on the 3.5 mm continuum. We found that the  $\text{NH}_2\text{D}$  peaks are not associated with either a dust continuum or an  $\text{NH}_3$  peak. For clumps G18.17, G18.21, G23.97N, and G23.98 in a prestellar stage, there are very weak

infrared and millimeter emissions that were blended with the  $\text{NH}_2\text{D}$  distributions. For clumps G23.44, G23.97S, and G25.38 in a protostellar stage, the  $\text{NH}_2\text{D}$  distributions are extended and surround the 3.5 mm peaks. Only for clump G25.71 (in a protostellar stage) is the  $\text{NH}_2\text{D}$  core located at the peak of the 3.5 mm continuum. It is likely that the 3.5 mm continuum core is just located in the background of  $\text{NH}_2\text{D}$  core along the line of sight.

Based on the temperature distributions of the dense cores, we found that the suitable habitat (or living environment) for  $\text{NH}_2\text{D}$  is 13–20 K, and the deuterium fractionations will reach a maximum at 16.5 K. For temperatures higher than 20 K, the activity of  $\text{NH}_2\text{D}$  is likely to be inhibited. At temperatures below 13 K,  $\text{NH}_2\text{D}$  may also tend to be frozen out on dust grains. However, we should also consider that the rotational temperature tracer,  $\text{NH}_3$ , may have been completely frozen onto the dust grain before  $\text{NH}_2\text{D}$ .

#### 4.2. N-bearing Species

Some N-bearing species are widely used as good tracers of dense gas and cold conditions for initial star formation, since they do not freeze out on dust grains in that condition (e.g., Suzuki et al. 2018; Awad & Shalabiea 2020; Peng et al. 2022).

However, different N-bearing species are slightly different in probing different physical conditions, relatively. In this work, we collect five N-bearing species: NH<sub>3</sub> (1, 1) and (2, 2), NH<sub>2</sub>D, H<sup>13</sup>CN, and HC<sup>15</sup>N. From the integrated emissions in Figures A1–A3, A5, and A6, NH<sub>3</sub> (1, 1) and (2, 2) are more widely distributed than others, while HC<sup>15</sup>N lines are much weaker and appear only at the peak positions of these samples. Furthermore, we detect almost no HC<sup>15</sup>N emission in the direction of G18.17, G18.21, G23.97N, and G23.98, which are at the relatively early star formation stage (or prestellar stages), but we detect HC<sup>15</sup>N emission in G23.44, G23.97S, G25.38, and G25.71, which are in a protostar stage. Therefore, HC<sup>15</sup>N may be tracing these evolved protostars. NH<sub>2</sub>D emissions are extended, but with an offset from the continuum and NH<sub>3</sub> peaks, so it can trace the earliest star-forming conditions among the five N-bearing species. H<sup>13</sup>CN emissions are distributed in an extended way and agree well with the peak position of the 3.5 mm continuum in all samples except G23.98. Therefore, H<sup>13</sup>CN may cover a relatively extensive evolutionary process from early to evolved stage.

Furthermore, Li et al. (2024) also found that NH<sub>2</sub>D and H<sup>13</sup>CN have different distributions with asymmetrically and resolvably distributed spatial structures in 11 of 18 sources, but the others have no significant differences. They think that this is mainly because of their limited spatial resolution and sensitivity. Actually, in our high-spatial-resolution and high-sensitivity observations, the emission distributions between the NH<sub>2</sub>D and H<sup>13</sup>CN are strongly different. This should result from their different habitats. The NH<sub>2</sub>D prefers to be located in colder conditions than the H<sup>13</sup>CN.

## 5. Summary

This work is a follow-up to Zhang et al. (2019, 2020), where we studied the gas dynamics, NH<sub>2</sub>D chemistry, and fragmentations in eight massive precluster and protocluster clumps, including G18.17, G18.21, G23.97N, G23.98, G23.44, G23.97S, G25.38, and G25.71. The observational data are from the high spatial resolution interferometric observations with the PdBI and the VLA. In this work, we present PdBI and the VLA spectral data including NH<sub>3</sub>, NH<sub>2</sub>D, H<sup>13</sup>CN, HC<sup>15</sup>N, SO, and C<sup>18</sup>O. We also study the possible habitats for these

tracers in the early stages of high-mass star formation. Some findings are following:

The NH<sub>3</sub> cores are in good agreement with the 3.5 mm emission peak, but the NH<sub>3</sub> is much more extended than the 3.5 mm emission structure. The NH<sub>2</sub>D cores are mainly located in the temperature range of 13.0–20.0 K, and the NH<sub>2</sub>D lines may be strongly depleted above 20 K. Comparing the column densities between NH<sub>2</sub>D and continuum cores, we found that the NH<sub>2</sub>D distributions are in a relatively diffuse condition. In these relatively early star formation conditions, we detect almost no HC<sup>15</sup>N emission in the direction of G18.17, G18.21, G23.97N, and G23.98, but we detect HC<sup>15</sup>N emission in G23.44, G23.97S, G25.38, and G25.71, which are in a protostar stage. It is likely that HC<sup>15</sup>N traces these evolved protostars. H<sup>13</sup>CN emissions are distributed in an extended way and agree well with the peak position of the 3.5 mm continuum in all samples except G23.98. The SO distributions agree well with the 3.5 mm peaks for the evolved star formation stage, except that the peak for G25.38 is offset from the 3.5 mm emission. However, we did not detect any SO emission in the four sources of the prestellar stage. We also found that at low temperatures ( $\leq 20$  K) and high densities ( $\gtrsim 10^6 \text{ cm}^{-3}$ ), the C<sup>18</sup>O molecule rapidly freezes onto the dust grains and becomes severely depleted. Based on the above, C<sup>18</sup>O is a poor tracer in conditions of very early star formation or prestellar cores, but C<sup>18</sup>O could be used to study diffuse ( $\lesssim 10^4 \text{ cm}^{-3}$ ) and warm ( $\gtrsim 20$  K) star formation regions.

## Acknowledgments

This work is supported by the National Key R&D Program of China (No. 2022YFA1602901), the local Science and Technology innovation projects of the central government (No. XZ202301YD0037C), and the National Natural Science Foundation of China (NSFC, grant No. 11933011). We also wish to thank the anonymous referee for comments that improved the clarity of the paper.

## Appendix Other Figure Materials

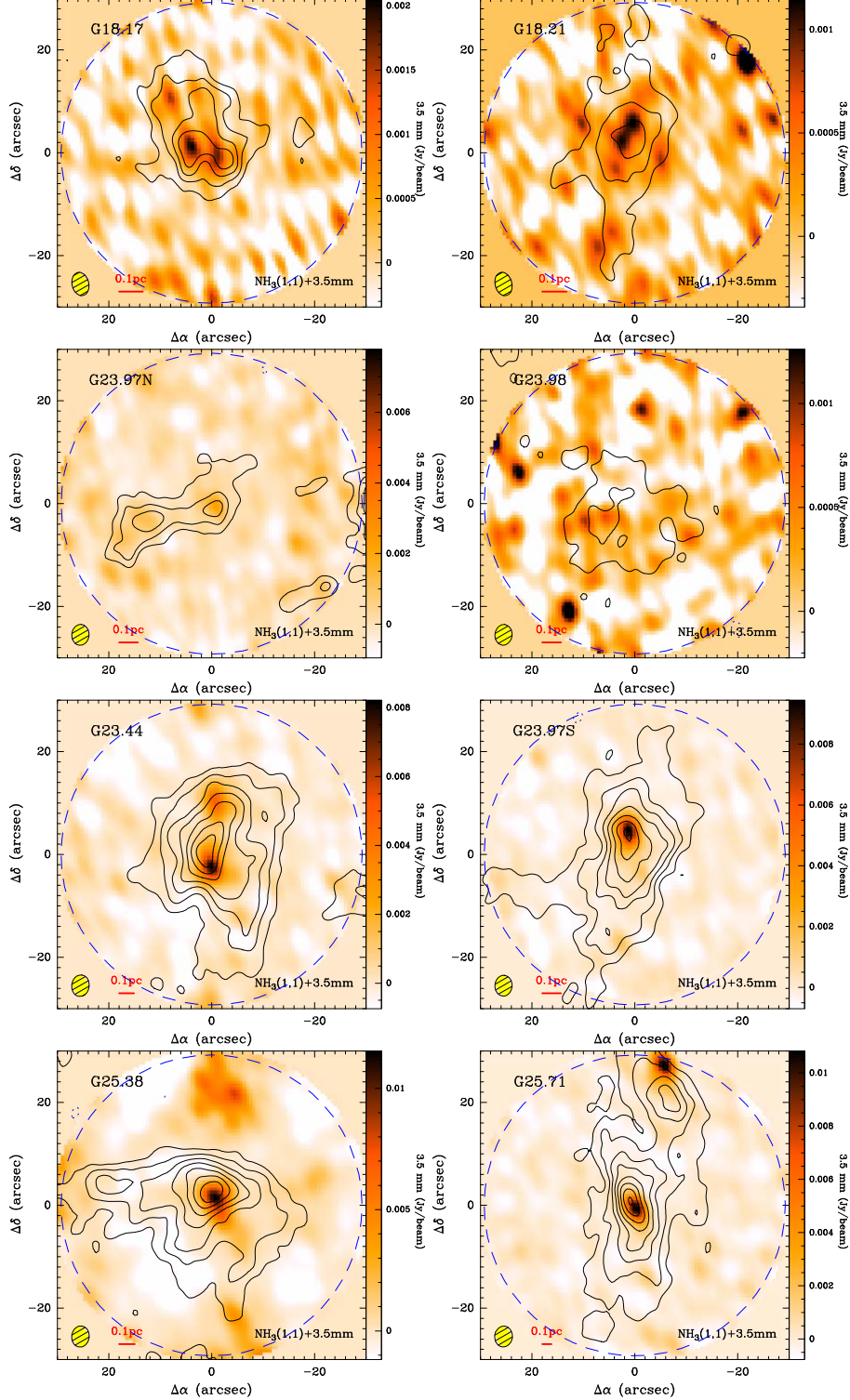


**Figure A1.**  $\text{NH}_3(1,1)$  integrated-intensity contours overlaid on 3.5 mm continuum emission with velocity range covering only the main line. The contour levels start at  $-3\sigma$  in steps of  $3\sigma$  for  $\text{NH}_3(1,1)$  with  $\sigma_{(a)-(h)} = 12.5, 20.2, 9.1, 9.8, 15.8, 12.6, 12.9, 10.2 \text{ mJy beam}^{-1} \text{ km s}^{-1}$ . The synthesized beam size of each subfigure is indicated at the bottom-left corner.

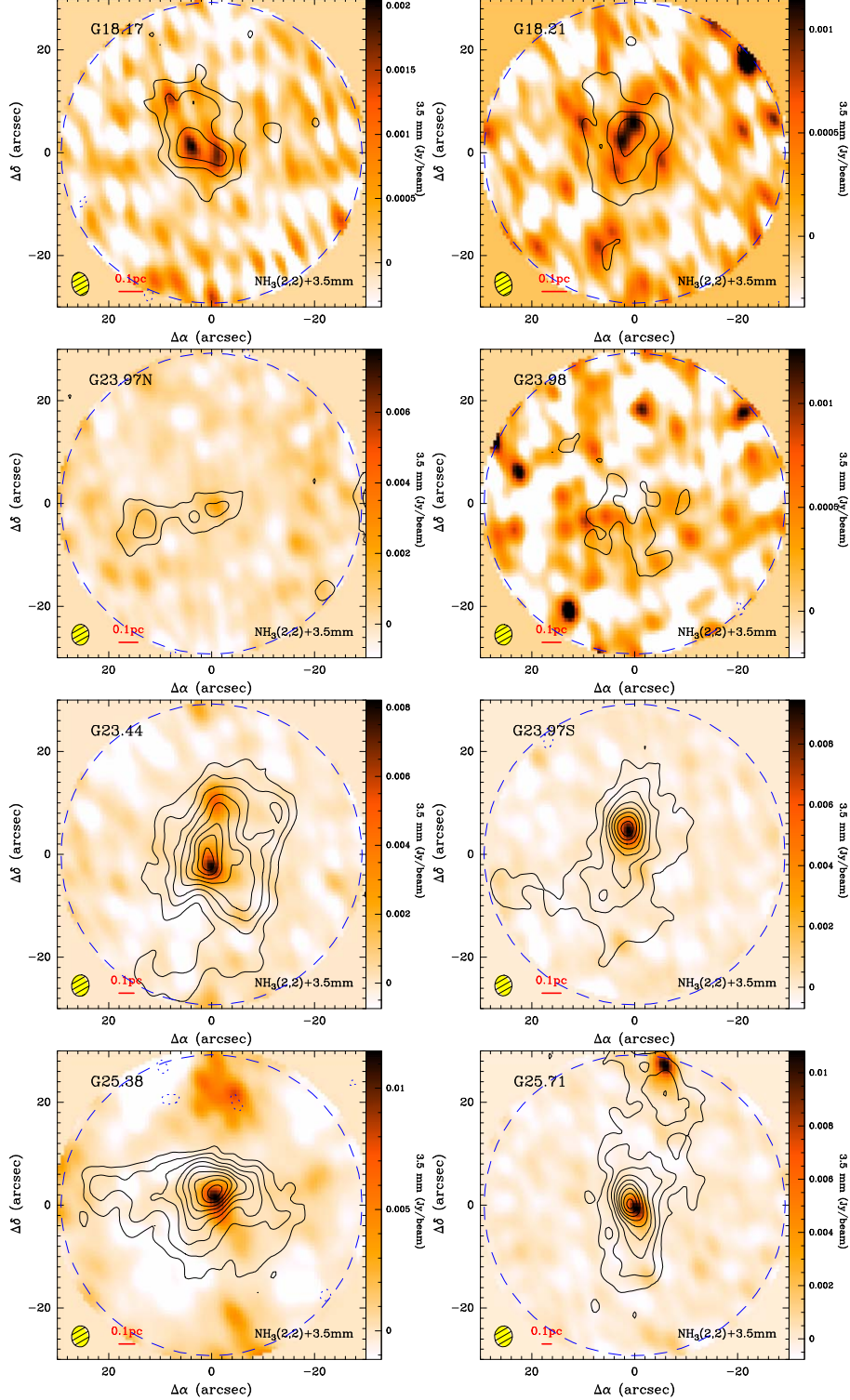


**Figure A2.**  $\text{NH}_3$  (2, 2) integrated-intensity contours overlaid on 3.5 mm continuum emission with velocity range covering only the main line. The contour levels start at  $-3\sigma$  in steps of  $3\sigma$  for  $\text{NH}_3$  (2, 2) with  $\sigma_{(\text{a})-(\text{h})} = 10.8, 13.5, 7.9, 7.2, 12.3, 8.2, 9.7, 8.3 \text{ mJy beam}^{-1} \text{ km s}^{-1}$ . The synthesized beam size of each subfigure is indicated at the bottom-left corner.

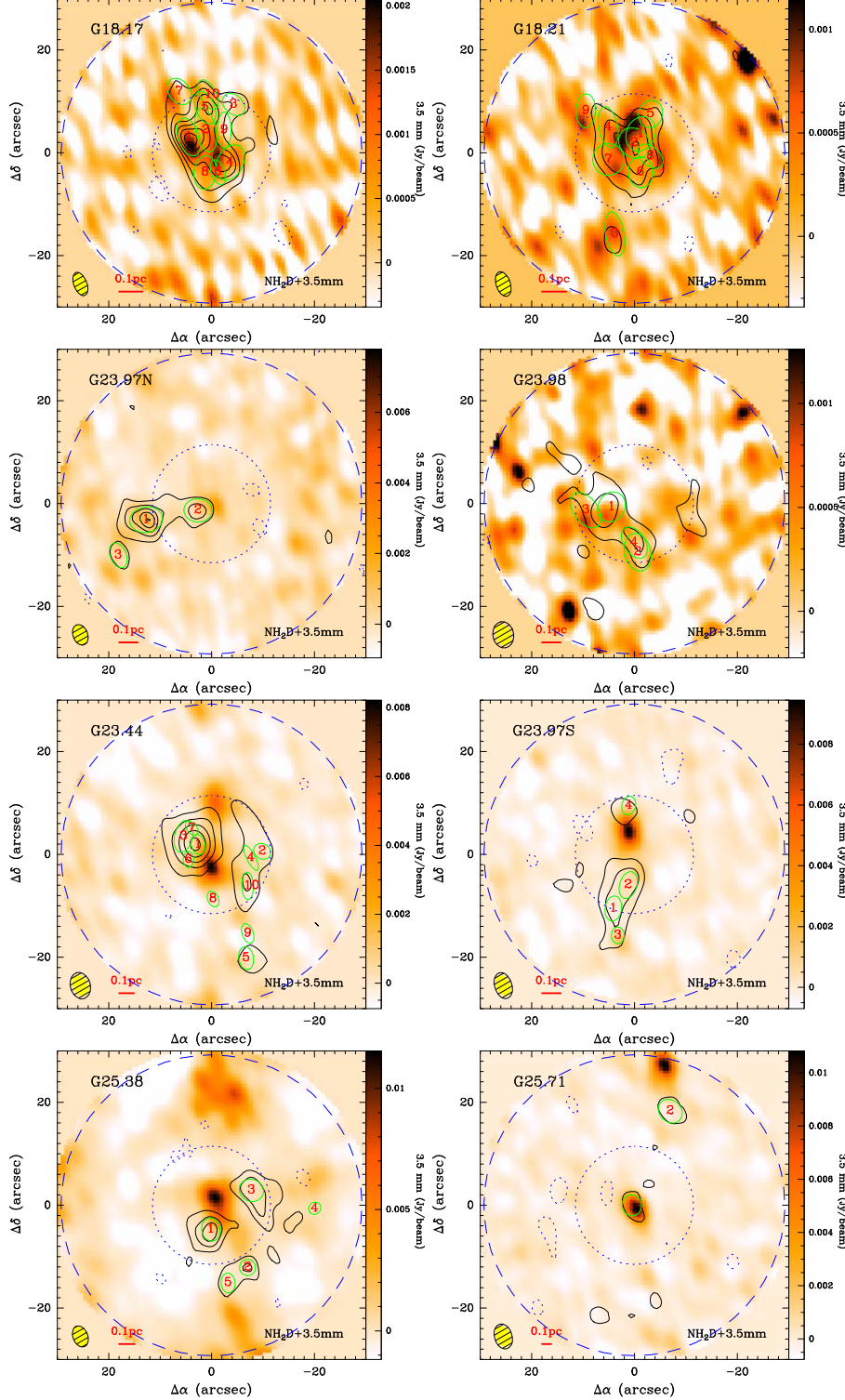


**Figure A3.**  $\text{NH}_2\text{D}$  integrated-intensity contours overlaid on 3.5 mm continuum emission with velocity range covering all the six HFS lines. The contour levels start at  $-3\sigma$  in steps of  $3\sigma$  for  $\text{NH}_2\text{D}$  with  $\sigma_{(a)-0} = 60.4, 60.9, 51.1, 53.2, 84.1, 48.3, 49.0, 50.4 \text{ mJy beam}^{-1} \text{ km s}^{-1}$ . The green numbers indicate the positions of extracted  $\text{NH}_2\text{D}$  cores and condensations. The synthesized beam size of each subfigure is indicated at the bottom-left corner.

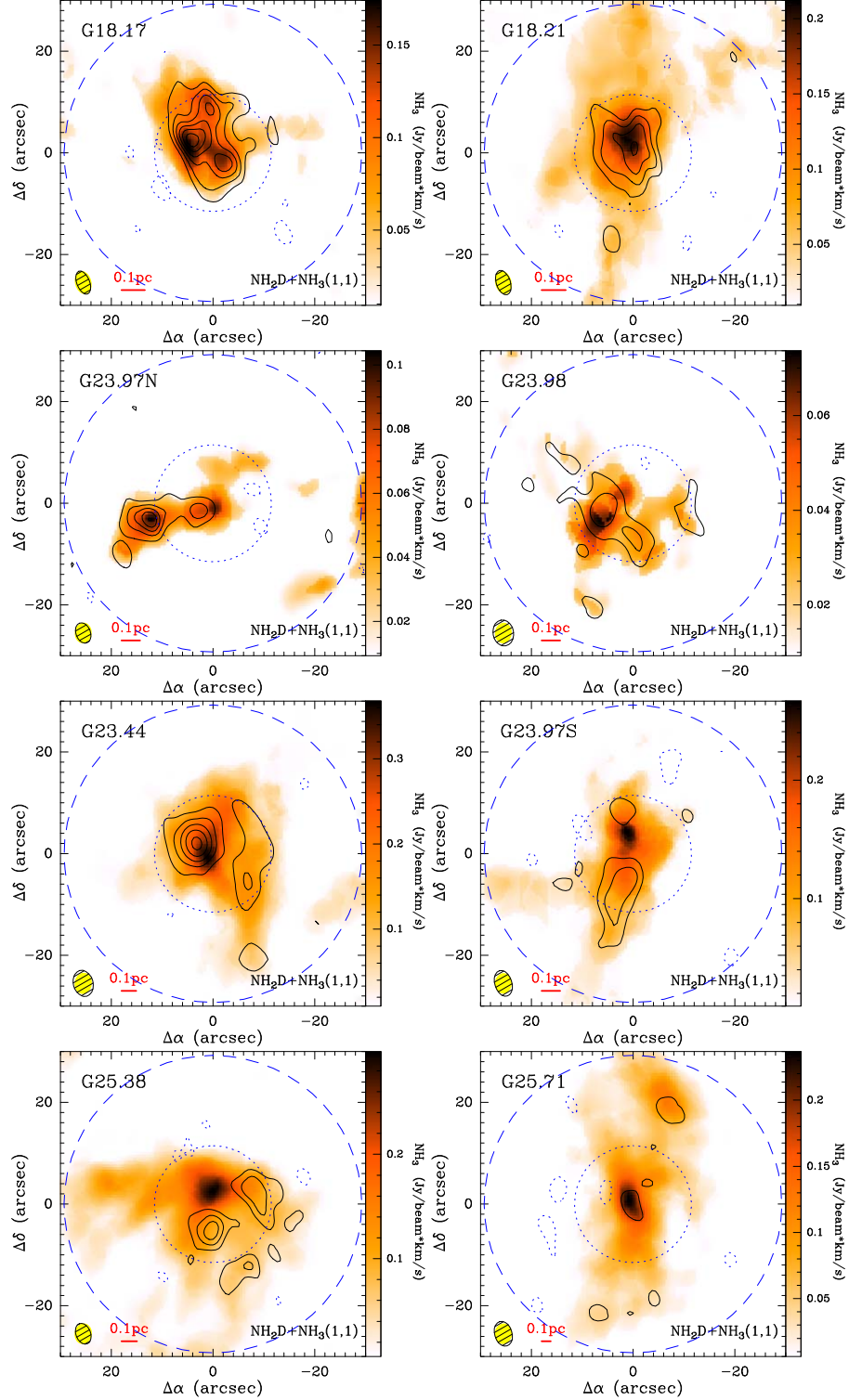


**Figure A4.**  $\text{NH}_2\text{D}$  integrated-intensity contours overlaid on an  $\text{NH}_3$  integrated-intensity image with velocity range covering all the six HFS lines. The contour levels start at  $-3\sigma$  in steps of  $3\sigma$  for  $\text{NH}_2\text{D}$  with  $\sigma_{(a)-(l)} = 60.4, 60.9, 51.1, 53.2, 84.1, 48.3, 49.0, 50.4 \text{ mJy beam}^{-1} \text{ km s}^{-1}$ . The synthesized beam size of each subfigure is indicated at the bottom-left corner.

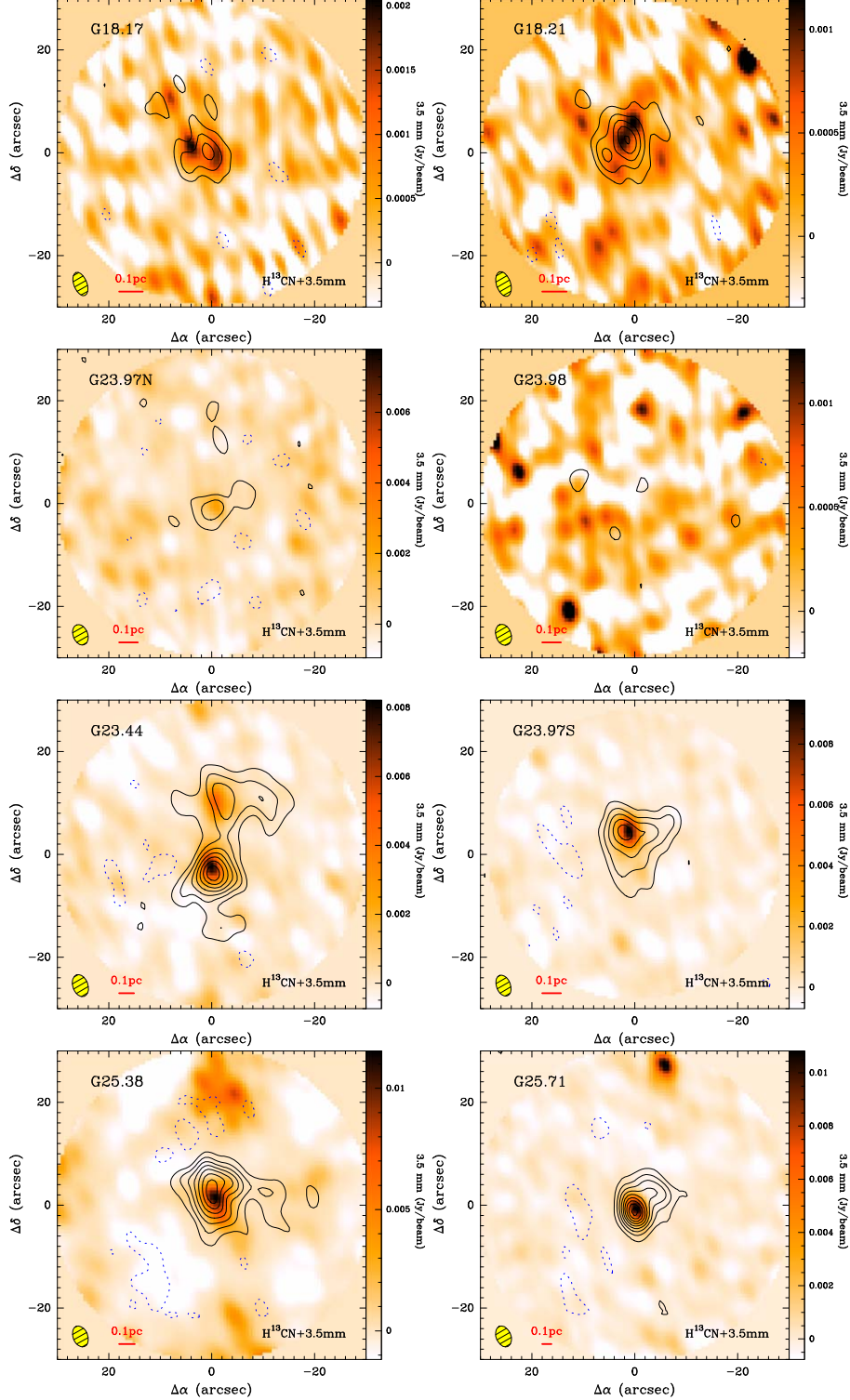


**Figure A5.**  $\text{H}^{13}\text{CN}$  integrated-intensity contours overlaid on 3.5 mm continuum emission with velocity range covering all the three HFS lines. The contour levels start at  $-3\sigma$  in steps of  $3\sigma$  for  $\text{H}^{13}\text{CN}$  with  $\sigma_{(a-l)} = 63.3, 58.4, 37.6, 60.9, 97.6, 73.0, 84.8, 90.1 \text{ mJy beam}^{-1} \text{ km s}^{-1}$ . The synthesized beam size of each subfigure is indicated at the bottom-left corner.

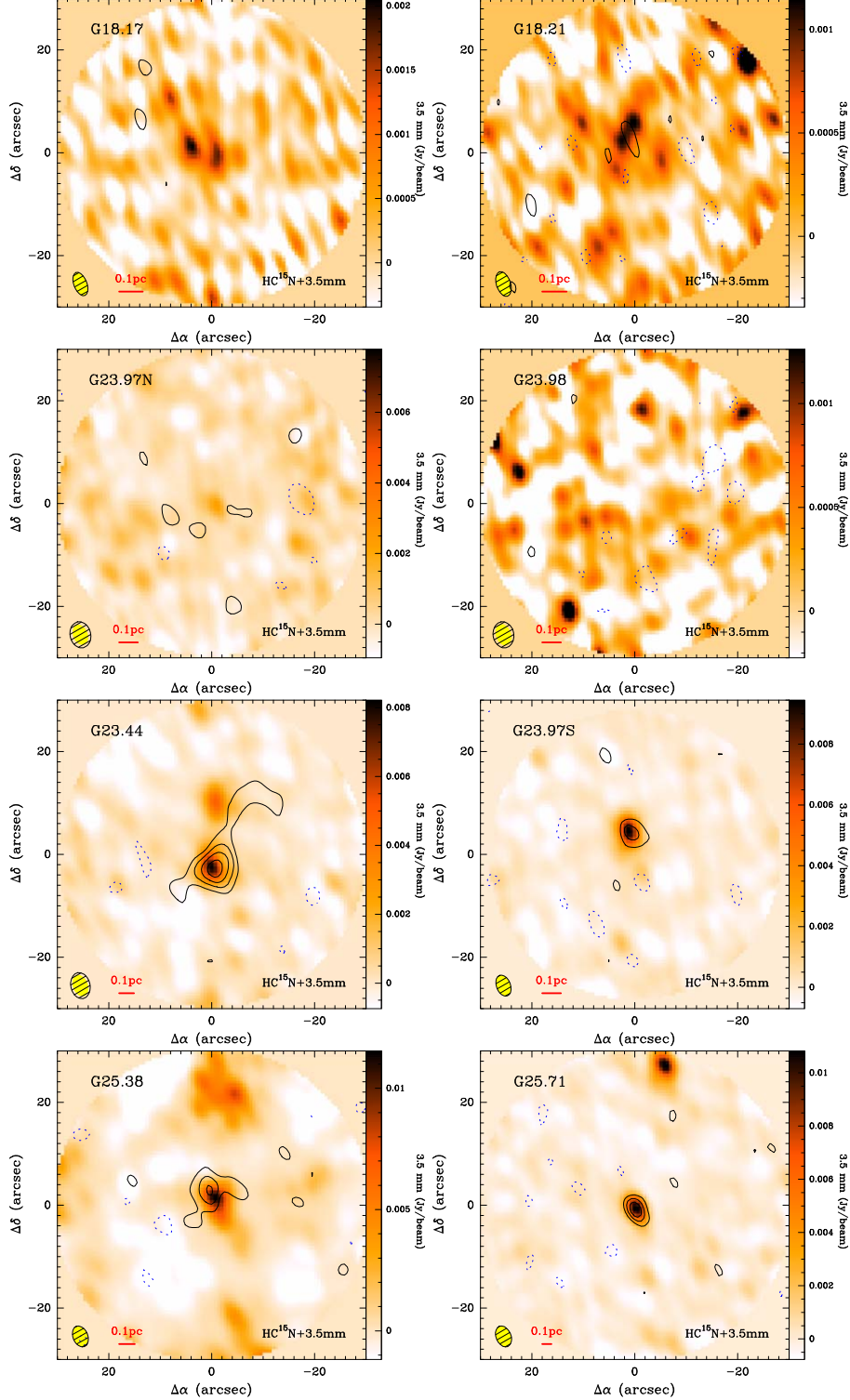


**Figure A6.** HC<sup>15</sup>N integrated-intensity contours overlaid on 3.5 mm continuum emission with velocity range covering only the emission line. The contour levels start at  $-3\sigma$  in steps of  $3\sigma$  for HC<sup>15</sup>N with  $\sigma_{(a-l)} = 88.5, 69.3, 73.8, 81.8, 61.4, 58.0, 55.1, 48.3$  mJy beam<sup>-1</sup> km s<sup>-1</sup>. The synthesized beam size of each subfigure is indicated at the bottom-left corner.

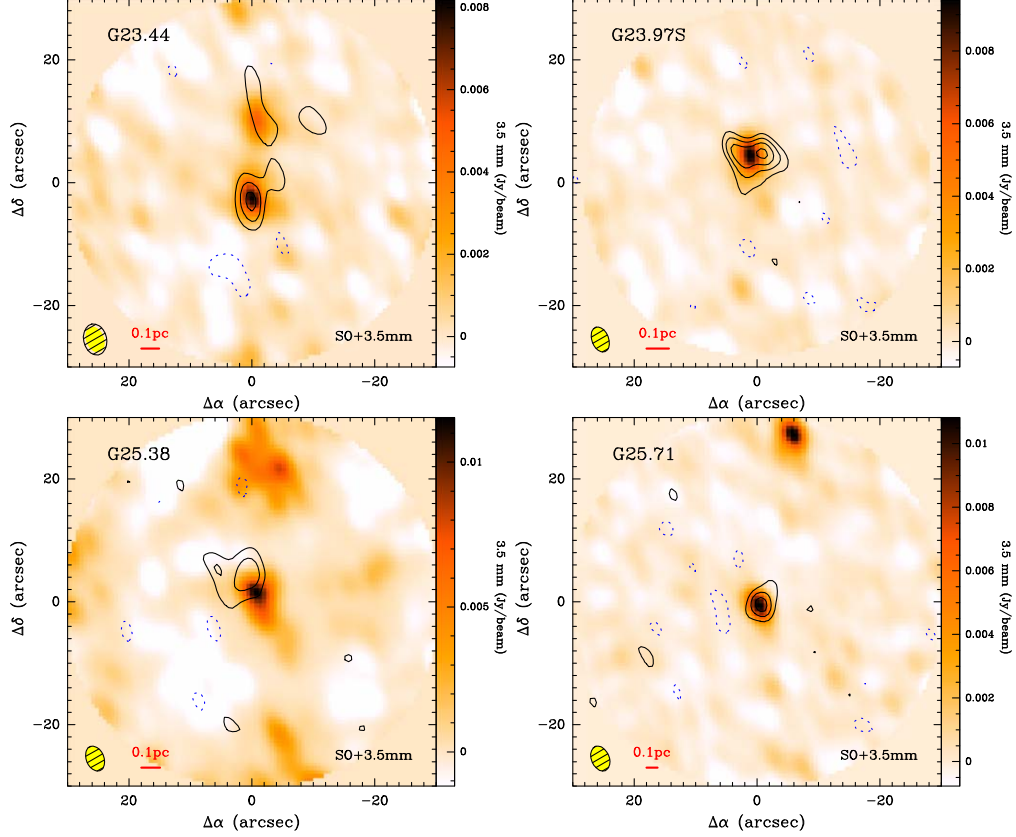


**Figure A7.** SO integrated-intensity contours overlaid on 3.5 mm continuum emission with velocity range covering only the emission line. The contour levels start at  $-3\sigma$  in steps of  $3\sigma$  for SO with  $\sigma_{(a)-(h)} = 71.4, 61.4, 52.1, 46.7 \text{ mJy beam}^{-1} \text{ km s}^{-1}$ . The synthesized beam size of each subfigure is indicated at the bottom-left corner.

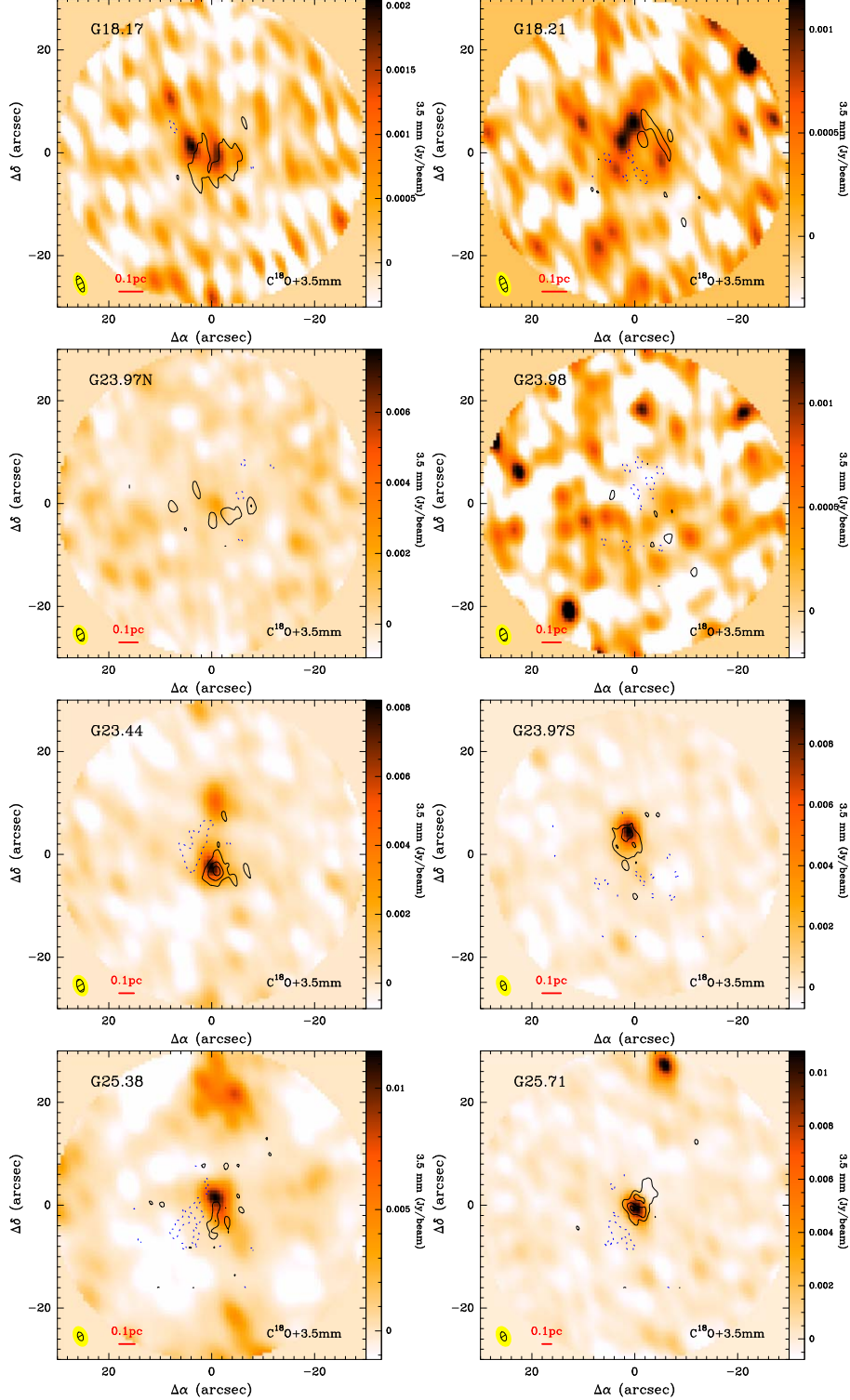


**Figure A8.**  $\text{C}^{18}\text{O}$  integrated-intensity contours overlaid on 3.5 mm continuum (BCD track) with velocity range covering only the emission line. The contour levels start at  $-3\sigma$  in steps of  $3\sigma$  for  $\text{C}^{18}\text{O}$  with  $\sigma_{(a)-(l)} = 330.3, 151.1, 185.1, 204.7, 520.1, 214.6, 184.9, 198.8 \text{ mJy beam}^{-1} \text{ km s}^{-1}$ . The synthesized beam size of each subfigure is indicated at the bottom-left corner.

## ORCID iDs

Chuan-Peng Zhang <https://orcid.org/0000-0002-4428-3183>

## References

Awad, Z., & Shalabiea, O. M. 2020, in Laboratory Astrophysics: From Observations to Interpretation, ed. F. Salama & H. Linnartz, Vol. 350 (Cambridge: IAU), 71

Bergin, E. A., & Tafalla, M. 2007, *ARA&A*, 45, 339

Booth, A. S., Walsh, C., & Ilee, J. D. 2019, *ARA&A*, 629, A75

Caselli, P., & Ceccarelli, C. 2012, *A&ARv*, 20, 56

Caselli, P., Vastel, C., Ceccarelli, C., et al. 2008, *A&A*, 492, 703

Ceccarelli, C., Caselli, P., Bockelée-Morvan, D., et al. 2014, Protostars and Planets VI (Tucson, AZ: Univ. Arizona Press), 859

Csengeri, T., Bontemps, S., Schneider, N., Motte, F., & Dib, S. 2011, *A&A*, 527, A135

Daniel, F., Coudert, L. H., Punanova, A., et al. 2016, *A&A*, 586, L4

Friesen, R. K., Di Francesco, J., Bourke, T. L., et al. 2014, *ApJ*, 797, 27

Gerner, T. 2014, PhD thesis, Ruprecht-Karls University of Heidelberg, Germany

Gerner, T., Shirley, Y. L., Beuther, H., et al. 2015, *A&A*, 579, A80

Ikeda, M., Hirota, T., & Yamamoto, S. 2002, *ApJ*, 575, 250

Li, Y., Wang, J., Li, J., et al. 2024, *MNRAS*, 527, 5049

Motte, F., Bontemps, S., & Louvet, F. 2018, *ARA&A*, 56, 41

Oliveira, C. M., Hébrard, G., Howk, J. C., et al. 2003, *ApJ*, 587, 235

Padovani, M., Walmsley, C. M., Tafalla, M., Hily-Blant, P., & Pineau Des Forêts, G. 2011, *A&A*, 534, A77

Peng, Y., Liu, T., Qin, S.-L., et al. 2022, *MNRAS*, 512, 4419

Pillai, T., Caselli, P., Kauffmann, J., et al. 2012, *ApJ*, 751, 135

Pillai, T., Kauffmann, J., Wyrowski, F., et al. 2011, *A&A*, 530, A118

Pillai, T., Wyrowski, F., Hatchell, J., Gibb, A. G., & Thompson, M. A. 2007, *A&A*, 467, 207

Roberts, H., & Millar, T. J. 2000, *A&A*, 361, 388

Rodgers, S. D., & Charnley, S. B. 2001, *ApJ*, 553, 613

Suzuki, T., Ohishi, M., Saito, M., et al. 2018, *ApJS*, 237, 3

Walmsley, C. M., Flower, D. R., & Pineau des Forêts, G. 2004, *A&A*, 418, 1035

Wielen, R., & Wilson, T. L. 1997, *A&A*, 326, 139

Wilson, T. L., & Rood, R. 1994, *ARA&A*, 32, 191

Zhang, C.-P., Csengeri, T., Wyrowski, F., et al. 2019, *A&A*, 627, A85

Zhang, C.-P., Li, G.-X., Pillai, T., et al. 2020, *A&A*, 638, A105

Zhang, C.-P., Wang, J.-J., Xu, J.-L., Wyrowski, F., & Menten, K. M. 2014, *ApJ*, 784, 107

Zhang, C.-P., Yuan, J.-H., Li, G.-X., Zhou, J.-J., & Wang, J.-J. 2017, *A&A*, 598, A76